

Nonequilibrium fluctuations of a quantum heat engine

Tobias Denzler,¹ Jonas F. G. Santos,² Eric Lutz,¹ and Roberto M. Serra²

¹*Institute for Theoretical Physics I, University of Stuttgart, D-70550 Stuttgart, Germany*

²*Centro de Ciências Naturais e Humanas, Universidade Federal do ABC, Avenida dos Estados 5001, 09210-580 Santo André, São Paulo, Brazil*

The thermodynamic properties of quantum heat engines are stochastic owing to the presence of thermal and quantum fluctuations. We here experimentally investigate the efficiency and nonequilibrium entropy production statistics of a spin-1/2 quantum Otto cycle. We first study the correlations between work and heat within a cycle by extracting their joint distribution for different driving times. We show that near perfect anticorrelation, corresponding to the tight-coupling condition, can be achieved. In this limit, the reconstructed efficiency distribution is peaked at the macroscopic efficiency and fluctuations are strongly suppressed. We further test the second law in the form of a joint fluctuation relation for work and heat. Our results characterize the statistical features of a small-scale thermal machine in the quantum domain and provide means to control them.

Heat engines have played a prominent role in our society since the industrial revolution. They are commonly used to generate motion by converting thermal energy into mechanical work [1]. An important figure of merit of heat engines is their efficiency, defined as the ratio of work output and heat input. According to the second law of thermodynamics, the maximum efficiency of any thermal motor operating between two heat baths is given by the Carnot formula, $\eta_{ca} = 1 - T_1/T_2$, where $T_{1,2}$ denote the respective temperatures of the cold and hot reservoirs [1]. For macroscopic heat engines consisting of a huge number of degrees of freedom, heat, work and, consequently, efficiency are deterministic quantities.

In the past decade, successful miniaturization has led to the experimental downscaling of thermal machines to microscopic [2–5] and nanoscopic [6–8] levels. Quantum heat engine operation has furthermore been reported recently in a variety of systems [9–14]. Contrary to macroscopic engines, small motors are subjected to thermal [15] and, at low enough temperatures, to additional quantum [16, 17] fluctuations. These are associated with random transitions between discrete energy levels, and thus introduce nonclassical features. As a result, heat, work, efficiency, and other relevant thermodynamic quantities such as the nonequilibrium entropy production, are stochastic variables. Such fluctuations strongly impact the performance of microscopic and nanoscopic machines [18–21]. Understanding their random properties is therefore essential. The efficiency statistics of classical Brownian heat engines has been studied experimentally with optically trapped colloidal particles in Refs. [4, 5]. Remarkably, efficiency fluctuations above the Carnot efficiency, which originate from negative entropy production events, have been observed [4, 5]. Meanwhile, the random entropy production for arbitrary heat engines has been theoretically predicted to satisfy a fluctuation relation [22–24], a fundamental nonequilibrium generalization of the second law of thermodynamics for small systems [15–17]. However, the efficiency and nonequilibrium entropy production statistics of quantum heat engines have not

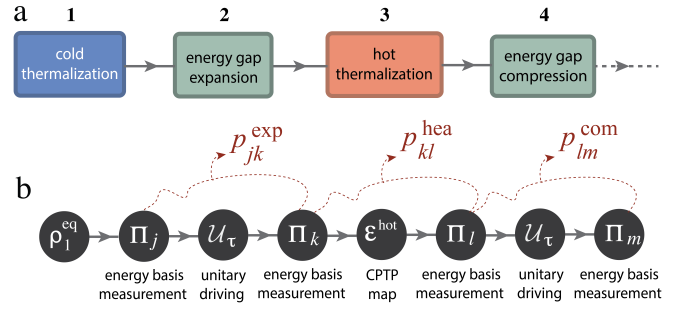


FIG. 1. Quantum heat engine. (a) Four steps (cooling, unitary expansion, heating, unitary compression) of the quantum Otto cycle realized in the experiment. (b) Multi-point-measurement scheme used to determine the joint distribution $P(W, Q)$ of work and heat: projective energy measurements are performed at the beginning (Π_j) and at the end (Π_k) of the expansion stroke, as well as at the beginning (Π_l) and at the end (Π_m) of the compression phase. Each pair of measurements is realized via a Ramsey-like interferometric method. The operator \mathcal{U}_τ describes unitary driving and ϵ^{hot} characterizes the completely positive trace preserving (CPTP) map that fully thermalizes the system to the hot temperature.

been explored experimentally so far.

We here report the study of the fluctuating properties of a quantum Otto engine [25] based on a driven nuclear spin-1/2 in a liquid state nuclear magnetic resonance (NMR) setup [26]. We extend existing interferometric methods [27–30] to extract the joint distribution of work and heat for different cycle times. We exploit the multipoint statistics to investigate the correlations between work and heat during an engine cycle, from the adiabatic to the nonadiabatic regime. We find near perfect anticorrelation, corresponding to the tight-coupling condition [31–34], in the quasiadiabatic limit. We additionally determine the distribution of the quantum stochastic efficiency and analyze the impact of the work-heat correlations on its features. We show, in particular, that, as the tight-coupling regime is approached, the random efficiency is peaked around the macroscopic efficiency, and

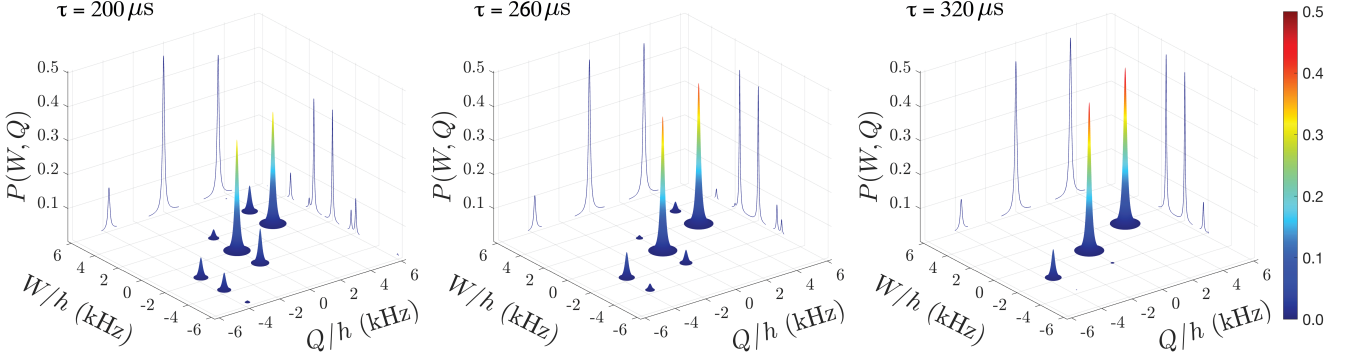


FIG. 2. Joint distribution of work and heat. Distribution $P(W, Q)$, Eq. (1), for three driving times, $\tau = 200, 260,$ and $320 \mu\text{s}$ in the unitary driving strokes. Experimental data is well fitted by nine Lorentz distributions at the corresponding pair of stochastic values for the extracted work ($W/h = 0, \pm 1.6, \pm 2.0 \pm 3.6, \pm 5.6$ kHz) and heat absorbed from the hot source ($Q/h = 0, \pm 3.6$ kHz). Diagonal peaks grow at the expense of off-diagonal ones as the quasiadiabatic regime is approached at $\tau = 320 \mu\text{s}$.

its fluctuations are strongly suppressed. We finally verify both a detailed and an integral bivariate quantum fluctuation relation for cyclic heat engine operation [22–24] that has not been tested before, and examine irreversible losses associated with quantum friction [35–37].

In our experiment, we use a ^{13}C -labeled CHCl_3 liquid sample diluted in Acetone- D_6 and a 500 MHz Varian NMR spectrometer. We employ the spin 1/2 of the ^{13}C nucleus as the working medium of the quantum heat engine and the ^1H nuclei as a heat bus to deliver heat to the machine. Work is performed by driving the heat engine with a resonant radio-frequency (rf) field. The low rf modes near to carbon resonance frequency further act as the cold heat bath, while high rf modes near the hydrogen Larmor frequency operate as the hot reservoir.

We realize a quantum Otto cycle that consists of four different steps [25] (Fig. 1a). 1) Cooling: the ^{13}C nuclear spin is initially cooled, using spatial average techniques [26], to a pseudo-thermal state $\rho_1^{\text{eq}} = \exp(-\beta_1 H_1^{\text{C}})/Z_1$ at cold inverse spin temperature β_1 , where H_1^{C} is the initial Hamiltonian and Z_1 the partition function. 2) Expansion: the machine is then driven by a time-modulated rf field on resonance with the ^{13}C nuclear spin. In a rotating frame at the ^{13}C Larmor frequency (≈ 125 MHz), the driving is described by the following effective Hamiltonian, $H_{\text{exp}}^{\text{C}}(t) = -(h\nu(t)/2) [\cos(\pi t/2\tau) \sigma_x^{\text{C}} + \sin(\pi t/2\tau) \sigma_y^{\text{C}}]$, where the nuclear spin energy gap, $h\nu(t) = h\nu_1(1 - t/\tau) + h\nu_2 t/\tau$ is varied linearly from $\nu_1 = 2.0$ kHz at time $t = 0$ to $\nu_2 = 3.6$ kHz at time $t = \tau$, where $\sigma_{x,y,z}^{\text{C}}$ are the Pauli spin operators of the ^{13}C nuclear spin. Implemented driving times ($\approx 10^{-4}$ s) are much shorter than the typical decoherence times in our setup (few seconds), implying that the corresponding evolution \mathcal{U}_τ is unitary to an excellent approximation [29]. 3) Heating: heat exchange between the ^{13}C and the ^1H nuclear spins, which was prepared at the hot inverse temperature β_2 [38], is achieved

by a sequence of free evolutions under the natural scalar interaction $H_J = (\pi/2)hJ\sigma_z^{\text{H}}\sigma_z^{\text{C}}$ (with $J \approx 215.1$ Hz) between both nuclei and rf pulses [12] (Supplementary Information). The resulting fully thermalized state is $\rho_2^{\text{eq}} = \exp(-\beta_2 H_2^{\text{C}})/Z_2$, with $H_2^{\text{C}} = H_{\text{exp}}^{\text{C}}(\tau)$. 4) Compression: we finally decrease the nuclear spin energy gap back to its initial value ν_1 in time τ according to $H_{\text{com}}^{\text{C}}(t) = -H_{\text{exp}}^{\text{C}}(\tau - t)$. In both cases, $\beta_i = (k_B T_i)^{-1}$, ($i = 1, 2$), where T_i is the spin temperature and k_B the Boltzmann constant.

Work and heat fluctuations of the quantum heat engine are characterized by a joint distribution $P(W, Q)$, which can be fully determined in the present experiment by a multipoint measurement scheme along the quantum Otto cycle for different driving times τ (Fig. 1b). The protocol consists of two projective energy measurements at the beginning (Π_j) and at the end (Π_k) of the expansion stroke, as well as two additional projective energy measurements at the beginning (Π_l) and at the end (Π_m) of the compression phase. Each of the three consecutive pairs of measurements is realized via a Ramsey-like interferometric method [27–30] and allows the determination of the respective transition probability. The corresponding joint distribution of the total extracted work W and the absorbed heat Q reads (Supplementary Information),

$$P(W, Q) = \sum_{j,k,l,m} \Delta(W, j, k, l, m, \tau, \gamma) \Delta(Q, j, k, l, m, \tau, \gamma) \times p_j^0 p_{jk}^{\text{exp}} p_{kl}^{\text{hea}} p_{lm}^{\text{com}}, \quad (1)$$

where $p_j^0 = \exp(-\beta_1 E_j^0)/Z^0$ is the occupation of the cold equilibrium state, with E_j^0 eigenenergies of H_1^{C} . The transition probabilities during expansion, heating and compression are respectively p_{jk}^{exp} , p_{kl}^{hea} and p_{lm}^{com} . Since the heating stroke leads to a hot equilibrium state, we simply have $p_{kl}^{\text{hea}} = p_l^\tau = \exp(-\beta_2 E_l^\tau)/Z^\tau$, independent of k , with E_l^τ eigenenergies of H_2^{C} . Occupation probabilities describe the effects of thermal fluctuations, while

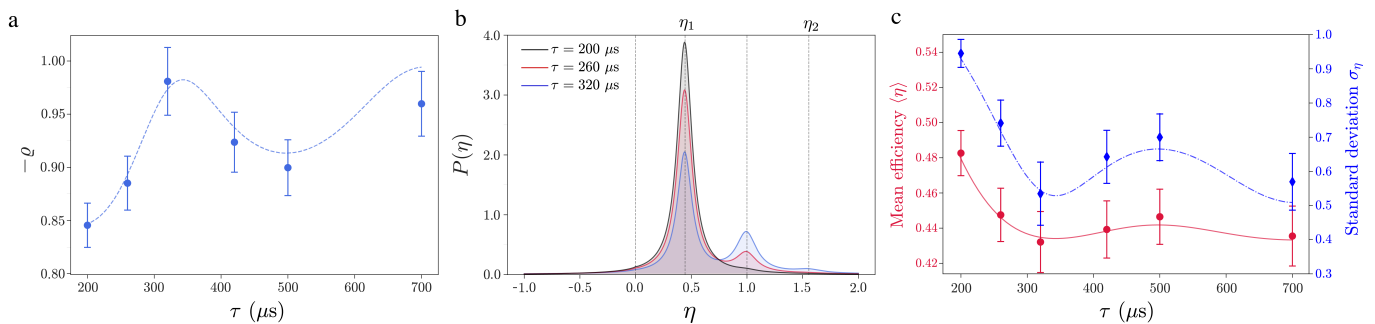


FIG. 3. Work-heat correlations and efficiency distribution. (a) Pearson correlation coefficient ρ for work and heat as a function of the driving time τ . (b) Efficiency distribution $P(\eta)$, Eq. (2), for three different driving times, displaying two large peaks at 1 and $\eta_1 = \eta_{\text{th}} \approx 0.44$, and two small peaks at 0 and $\eta_2 = 2 - \eta_{\text{th}} \approx 1.56$. (c) Mean microscopic efficiency $\langle \eta \rangle$ and corresponding standard deviation σ_η as a function of the driving time τ . Work and heat are maximally anticorrelated as the tight-coupling condition is approached for $\tau = 320 \mu\text{s}$. As a result, the stochastic efficiency is sharply peaked around the macroscopic efficiency η_{th} and the standard deviation, which quantifies fluctuations, strongly decreases. By contrast, the mean microscopic efficiency decreases. Symbols are the experimental data and lines show theoretical predictions.

transition probabilities those of quantum fluctuations and quantum dynamics [39]. For ideal projective measurements, each spectral peak is infinitely sharp ($\gamma = 0$), and energy changes during single strokes are given by differences of energy eigenvalues [40]. In this case, the two functions Δ associated with work and heat, $X = (W, Q)$, are $\Delta(X, j, k, l, m, \tau, 0) = \delta(X - x_{jklm})$, with $w_{jklm} = E_j^0 - E_k^\tau + E_m^\tau - E_l^0$ and $q_{jklm} = E_l^\tau - E_m^\tau$. However, the experimental Ramsey-like interferometric scheme leads to spectral peaks with a finite width γ , which are well fitted by a Lorentzian distribution, $\Delta(X, j, k, l, m, \tau, \gamma) = 1/\{\pi\gamma[1 + (X - x_{jklm})^2/\gamma^2]\}$ [29, 30].

Examples of experimentally reconstructed bivariate distributions for work and heat are shown in Fig. 2 for three different driving times, for $k_B T_1/h = 1.60 \pm 0.02$ kHz and $k_B T_2/h = 12.21 \pm 0.89$ kHz (results for additional driving times are presented in the Supplementary Information). We observe up to nine discrete Lorentzian peaks, each with a width of about 0.15 kHz. As the driving time increases from $\tau = 200 \mu\text{s}$ to $\tau = 320 \mu\text{s}$, diagonal peaks grow at the expense of off-diagonal ones. This suggests that work-heat correlations are enhanced as the process becomes more and more adiabatic.

Work-heat correlations within the heat engine cycle are conveniently studied quantitatively with the help of the Pearson coefficient, $\rho = \text{cov}(W, Q)/\sigma_W \sigma_Q$, defined as the ratio of the covariance and the respective standard deviations [41]. Work and heat are in general (strongly) anticorrelated ($\rho < 0$) for the quantum Otto engine (Fig. 3a) and correlations oscillate as a function of time, owing to the periodic nature of the driving during expansion and compression steps; dots represent experimental data and the dashed line a numerical simulation (Supplementary Information). Maximum anticorrelation ($\rho \simeq -1$) is achieved for quasiadiabatic driving for $\tau = 320 \mu\text{s}$. In this limit, the quantum heat engine satisfies the tight-coupling condition [31–34], which implies that work and

heat are proportional to each other. The tight-coupling condition plays a special role in the investigation of the universal properties of heat engines [31–34].

We next move to the analysis of the quantum stochastic efficiency defined as $\eta = W/Q$ for each single realization [42]. This (random) quantity should not be confused with the (deterministic) thermodynamic efficiency, $\eta_{\text{th}} = \langle W \rangle / \langle Q \rangle$, which is given in terms of averages [1]. In the case of adiabatic driving, the latter reduces to the standard Otto efficiency, $\eta_{\text{Otto}} = 1 - \nu_1/\nu_2$ [25]. The efficiency distribution $P(\eta)$ follows from the joint distribution (1) via integration over all work and heat values,

$$P(\eta) = \iint dW dQ \delta\left(\eta - \frac{W}{Q}\right) P(W, Q). \quad (2)$$

The corresponding experimental distribution is displayed in Fig. 3b for three different driving times. We identify four Lorentzian-like peaks: two (large) peaks found at 1 and $\eta_1 = \eta_{\text{th}}$, and two (small) peaks located at 0 and $\eta_2 = 2 - \eta_{\text{th}}$ (Supplementary Information). The stochastic efficiency is further seen to take values above 1 and below 0. In the former case, the produced random work is larger than the absorbed stochastic heat, while in the latter case work is added to the machine or heat is given to the hot bath. These results indicate that all values of the stochastic efficiency are possible in a small-scale quantum engine running in finite time, including those forbidden by the macroscopic second law. As the driving time approaches the adiabatic regime ($\tau = 320 \mu\text{s}$), we observe that the macroscopic efficiency η_{th} becomes increasingly more likely. In order to examine the properties of the random microscopic efficiency η , we evaluate its mean $\langle \eta \rangle$ and standard deviation σ_η in the interval $[-5, 5]$ (Fig. 3c). The behavior of the mean efficiency and of its standard deviation as a function of τ is exactly opposite to that of the Pearson coefficient (Fig. 3a): they decrease when the correlations increase, and vice

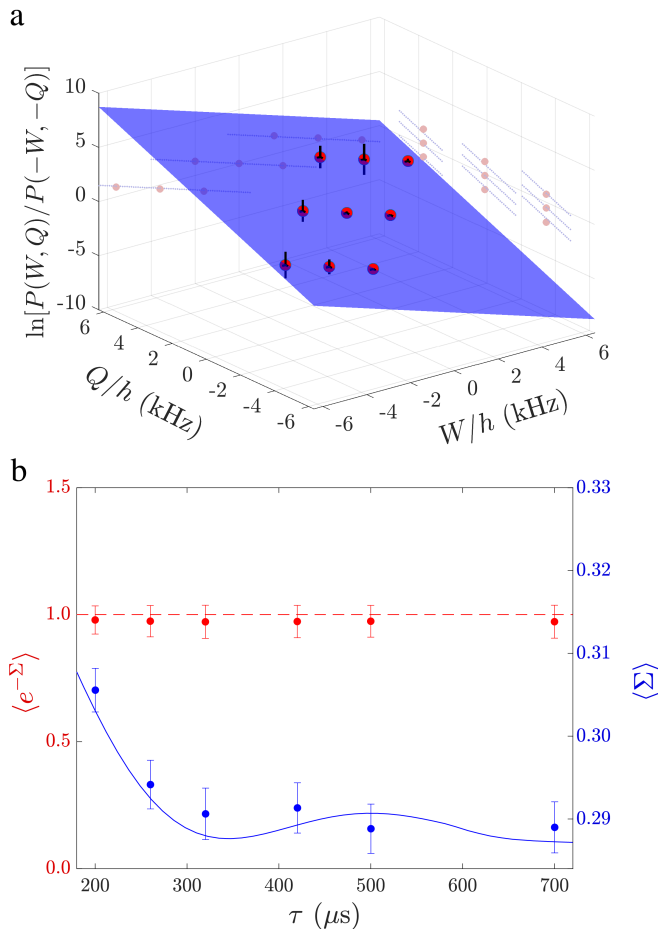


FIG. 4. Nonequilibrium quantum fluctuation relations. (a) Verification of the detailed fluctuation relation (3) for the quantum Otto cycle: the values of $\ln[P(W, Q)/P(-W, -Q)]$ (red dots) should lie within the (blue) plane defined by the total entropy production $z = \Sigma = \Delta\beta Q - \beta_1 W$; the dashed blue lines show the respective projections of the plane on the work and heat axes. (b) Confirmation of the integral fluctuation theorem, $\langle \exp(-\Sigma) \rangle = 1$, (red dots) and average entropy production $\langle \Sigma \rangle$ (blue dots) as a function of the driving time τ . Irreversible losses are minimal when the tight-coupling condition is approached for $\tau = 320\mu\text{s}$.

versa, revealing the strong relationship existing between the work-heat (anti)correlations and the features of the stochastic efficiency. Surprisingly, the dependence of the mean microscopic efficiency $\langle \eta \rangle$ on τ is at variance with that of the macroscopic efficiency η_{th} (Supplementary Information). The microscopic efficiency is thus larger for nonadiabatic driving than for adiabatic driving; this is due to the peaks above η_{th} and, thus, to events violating the macroscopic second law which are more likely for nonadiabatic driving. We also note that the stochastic efficiency tends to the (deterministic) macroscopic efficiency η_{th} as the tight-coupling limit is approached. The effects of fluctuations are here significantly suppressed due to the strong work-heat anticorrelation, even though

these fluctuations do not vanish [42].

Energy fluctuations in a heat engine cycle are predicted to obey a detailed fluctuation relation of the form [22–24],

$$\frac{P(W, Q)}{P(-W, -Q)} = e^{\Delta\beta Q - \beta_1 W}, \quad (3)$$

where $\Delta\beta = \beta_1 - \beta_2$ and $P(-W, -Q)$ is the joint distribution of measuring $(-W, -Q)$ in the reverse operation of the engine. An integral fluctuation theorem, $\langle \exp(-\Sigma) \rangle = \iint dW dQ P(W, Q) \exp(-\Sigma) = 1$, for the entropy production $\Sigma = \Delta\beta Q - \beta_1 W$ follows after integration over one cycle [22–24]. The latter expression may be regarded as a nonequilibrium generalization of the Carnot formula, $\langle W \rangle / \langle Q \rangle \leq 1 - T_1/T_2$, which can be derived from it by applying Jensen’s inequality [22–24]. Figure 4a displays a verification of the quantum detailed fluctuation relation (3) for $\tau = 200 \mu\text{s}$ (see Supplementary Information for other driving times). We witness very good agreement between the experimental values of $\ln[P(W, Q)/P(-W, -Q)]$ (red dots) and the predictions of Eq. (3) indicated by the (blue) plane $z = \Sigma$, the z -axis being vertical. A confirmation of the integral fluctuation theorem, $\langle \exp(-\Sigma) \rangle = 1$, is further shown in Fig. 4b, as a function of the driving time, together with the average entropy production $\langle \Sigma \rangle$, which characterizes irreversible losses within the cycle. Since the two driving Hamiltonians, $H_{\text{exp}}^C(t)$ and $H_{\text{com}}^C(t)$, do not commute at different times, the heat engine exhibits internal friction associated with nonadiabatic transitions between the instantaneous eigenstates of the ^{13}C nuclear spin [35–37]. This purely quantum friction mechanism is the source of irreversibility in the quantum Otto cycle, depending on the driving speed: the mean entropy production $\langle \Sigma \rangle$ decreases as the adiabatic regime is approached (Fig. 4b), and vice versa. We also note a marked connection between quantum friction (Fig. 4b) and work-heat correlations (Fig. 3a), which has not been acknowledged before.

In conclusion, we have performed the first experimental study of the work-heat correlations and their strong impact on both efficiency and entropy production statistics of a quantum heat engine. We have shown that the tight-coupling condition, corresponding to maximum work-heat anticorrelation, can be reached for finite-time quasiadiabatic driving. In this regime, the stochastic efficiency reduces to the macroscopic efficiency, and both thermal and quantum fluctuations are notably suppressed. We have additionally observed that macroscopic and microscopic efficiencies display opposite behavior, due to random events violating the macroscopic second law. We have finally confirmed nonequilibrium generalizations of the Carnot formula in the form of bivariate fluctuation relations for work and heat, and analyzed the effect of quantum friction on the total entropy production. Our findings give a unique insight into the nonequilibrium fluctuating properties of small quantum thermal machines and provide direct means to control them.

SUPPLEMENTAL MATERIALS

This Supplementary Information provides additional details on the experimental protocol, the determination of the joint distribution for work and heat, and the analysis of the experimental data.

Thermal states initialization

Spatial average techniques [26, 29, 30, 38] were used to initialize the engine states, which are local pseudo-thermal states encoded in the ^1H and ^{13}C nuclei. We present in Table I the populations and the respective local spin temperatures in the eigenbasis of Hamiltonians \mathcal{H}_0^{H} and \mathcal{H}_0^{C} .

^1H nucleus	p_0^{H}	p_1^{H}	$k_B T_2$ (peV)
	0.67 ± 0.01	0.33 ± 0.01	21.5 ± 0.4
^{13}C nucleus	p_0^{C}	p_1^{C}	$k_B T_1$ (peV)
	0.78 ± 0.01	0.22 ± 0.01	6.6 ± 0.1

TABLE I. Populations and spin temperatures of the initial states of the ^1H and ^{13}C nuclei. The corresponding off-diagonal elements are zero within the measurement errors.

Compression and expansion protocols

The energy gap compression and expansion protocols are implemented with a time-modulated amplitude and phase transverse rf-pulse on resonance with the ^{13}C nuclear spin in order to produce effectively the time-dependent driving Hamiltonian $\mathcal{H}^{\text{C}}(\tau)$ described in the main text. The intensities of the transverse field at the beginning and end of the driving protocol were properly calibrated in order to have the associated frequencies given in the main text. The duration of the modulated transverse pulse was varied from 100 μs to 700 μs in different implementations of the quantum heat engine cycle.

Heating protocol

The thermalization process used to heat the ^{13}C nuclear spin of the quantum Otto engine during the second stroke has the local effect of a linear non-unitary map $\varepsilon(\rho_j) = \text{Tr}_{k \neq j} [\mathcal{U}_\tau (\rho_H^0 \otimes \rho_C^0) \mathcal{U}_\tau^\dagger]$, with $(j, k) = (H, C)$. It is represented by the following set of maps [38]

$$\varepsilon(\rho_j) = \sum_{\ell=1}^4 K_\ell \rho_j^0 K_\ell^\dagger, \quad (4)$$

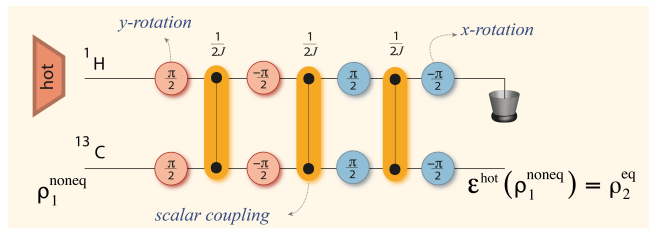


FIG. 5. NMR pulse sequence used in the heat exchange protocol. The outcome of this sequence (which takes about 7 ms) is an effective full thermalization described by a completely positive trace preserving (CPTP) map on reduced density operator of the carbon nucleus, $\varepsilon^{\text{hot}} : \rho_1^{\text{noneq}} \rightarrow e^{-\beta_2 H_2^{\text{C}}} / Z_2$, leading it to an equilibrium state at the hot inverse temperature β_2 . Orange connections represent free evolutions under the scalar interaction during the time displayed above the symbol. Blue (red) circles stand for x (y) rotations by the displayed angle implemented by transverse rf pulses.

History	stroke 1	stroke 2	stroke 3	stroke 4	$W/h \pm 0.15$ (kHz)	$Q/h \pm 0.15$ (kHz)
1	$ \Psi_-^1\rangle$	$ \Psi_-^2\rangle$	$ \Psi_-^2\rangle$	$ \Psi_-^1\rangle$	0	0
2	$ \Psi_-^1\rangle$	$ \Psi_-^2\rangle$	$ \Psi_-^2\rangle$	$ \Psi_+^1\rangle$	-2.0	0
3	$ \Psi_-^1\rangle$	$ \Psi_-^2\rangle$	$ \Psi_+^2\rangle$	$ \Psi_-^1\rangle$	3.6	3.6
4	$ \Psi_-^1\rangle$	$ \Psi_-^2\rangle$	$ \Psi_+^2\rangle$	$ \Psi_+^1\rangle$	1.6	3.6
5	$ \Psi_-^1\rangle$	$ \Psi_+^2\rangle$	$ \Psi_-^2\rangle$	$ \Psi_-^1\rangle$	-3.6	-3.6
6	$ \Psi_-^1\rangle$	$ \Psi_+^2\rangle$	$ \Psi_-^2\rangle$	$ \Psi_+^1\rangle$	-5.6	-3.6
7	$ \Psi_-^1\rangle$	$ \Psi_+^2\rangle$	$ \Psi_+^2\rangle$	$ \Psi_-^1\rangle$	0	0
8	$ \Psi_-^1\rangle$	$ \Psi_+^2\rangle$	$ \Psi_+^2\rangle$	$ \Psi_+^1\rangle$	-2.0	0
9	$ \Psi_+^1\rangle$	$ \Psi_-^2\rangle$	$ \Psi_-^2\rangle$	$ \Psi_-^1\rangle$	2.0	0
10	$ \Psi_+^1\rangle$	$ \Psi_-^2\rangle$	$ \Psi_-^2\rangle$	$ \Psi_+^1\rangle$	0	0
11	$ \Psi_+^1\rangle$	$ \Psi_-^2\rangle$	$ \Psi_+^2\rangle$	$ \Psi_-^1\rangle$	5.6	3.6
12	$ \Psi_+^1\rangle$	$ \Psi_-^2\rangle$	$ \Psi_+^2\rangle$	$ \Psi_+^1\rangle$	3.6	3.6
13	$ \Psi_+^1\rangle$	$ \Psi_+^2\rangle$	$ \Psi_-^2\rangle$	$ \Psi_-^1\rangle$	-1.6	-3.6
14	$ \Psi_+^1\rangle$	$ \Psi_+^2\rangle$	$ \Psi_-^2\rangle$	$ \Psi_+^1\rangle$	-3.6	-3.6
15	$ \Psi_+^1\rangle$	$ \Psi_+^2\rangle$	$ \Psi_+^2\rangle$	$ \Psi_-^1\rangle$	2.0	0
16	$ \Psi_+^1\rangle$	$ \Psi_+^2\rangle$	$ \Psi_+^2\rangle$	$ \Psi_+^1\rangle$	0	0

TABLE II. All transition histories between the instantaneous eigenstates $|\Psi_\pm^i\rangle$ ($i = 1, 2$) for each stroke of the heat engine, together with the corresponding values of work and heat.

with the Kraus operators

$$K_1 = \sqrt{1-p} \begin{pmatrix} 1 & 0 \\ 0 & 0 \end{pmatrix}, K_2 = \sqrt{p} \begin{pmatrix} 0 & 0 \\ 0 & 1 \end{pmatrix} \quad (5)$$

$$K_3 = \sqrt{1-p} \begin{pmatrix} 0 & 1 \\ 0 & 0 \end{pmatrix}, K_4 = \sqrt{p} \begin{pmatrix} 0 & 0 \\ -1 & 0 \end{pmatrix}. \quad (6)$$

The parameter p denotes the population of the excited state in the Hydrogen nucleus. The above Kraus operators correspond to the generalized amplitude damping of a single-1/2 system. From a local point of view, the map thus implements complete thermalization. The NMR pulse sequence used in the heat exchange protocol in the experiment is shown in Fig. 5, where the Hydrogen nucleus is used as a heat bus.

Joint distribution for work and heat - theory

The joint distribution for the total work W and the absorbed heat Q may be determined by performing energy measurements on the engine at the beginning and at the end of the expansion, heating and compression strokes [42], as depicted in Fig. 1b of the main text. We first consider the case of ideal projective measurements. By performing projective energy measurements at the beginning and at the end of the expansion step, the distribution of the expansion work W_2 reads [40],

$$P(W_2) = \sum_{j,k} \delta [W_2 - (E_k^\tau - E_j^0)] p_{jk}^{\text{exp}} p_j^0, \quad (7)$$

where E_j^0 and E_k^τ are the respective initial and final energy eigenvalues, $p_j^0 = \exp(-\beta_1 E_j^0)/Z^0$ is the initial thermal occupation probability with partition function Z^0 and $p_{jk}^{\text{exp}} = |\langle j | U_{\text{exp}}(\tau) | k \rangle|^2$ denotes the transition probability between the instantaneous eigenstates $|j\rangle$ and $|k\rangle$ in time τ with the corresponding unitary U_{exp} .

Similarly, the probability density of the heat $Q = Q_3$ during the following heating step, given the expansion work W_2 , is equal to the conditional distribution [43],

$$P(Q|W_2) = \sum_{i,l} \delta [Q - (E_l^\tau - E_i^\tau)] p_{il}^{\text{hea}} p_i^\tau, \quad (8)$$

where the occupation probability at time τ is $p_i^\tau = \delta_{ki}$ when the system is in eigenstate $|k\rangle$ after the second projective energy measurement.

The quantum work distribution for compression, given the expansion work W_2 and the heat Q , is additionally,

$$P(W_4|Q, W_2) = \sum_{r,m} \delta [W_4 - (E_m^0 - E_r^\tau)] p_{rm}^{\text{com}} p_r^\tau, \quad (9)$$

with the occupation probability $p_r^\tau = \delta_{rl}$ when the system is in eigenstate $|l\rangle$ after the third projective energy measurement. The transition probability $p_{rm}^{\text{com}} = |\langle r | U_{\text{com}}(\tau) | m \rangle|^2$ is fully specified by the unitary time evolution operator for compression U_{com} .

The joint probability of having certain values of W_4 , Q and W_2 during a cycle of the quantum engine now follows from the chain rule for conditional probabilities, $P(W_4, Q, W_2) = P(W_4|Q, W_2)P(Q|W_2)P(W_2)$ [44]. Using Eqs. (7), (8) and (9), we find,

$$\begin{aligned} P(W_2, Q, W_4) &= \sum_{j,k,l,m} \delta [W_2 - (E_k^\tau - E_j^0)] \\ &\times \delta [Q - (E_l^\tau - E_i^\tau)] \delta [W_4 - (E_m^0 - E_r^\tau)] \\ &\times p_j^0 p_{jk}^{\text{exp}} p_{kl}^{\text{hea}} p_{lm}^{\text{com}}. \end{aligned} \quad (10)$$

Introducing the total extracted work $W = -(W_2 + W_4)$ work and integrating over all work values W_2 and W_4 ,

the joint distribution for work and heat is given by,

$$P(W, Q) = \int dW_2 dW_4 \delta[W + (W_2 + W_4)] P(W_2, Q, W_4). \quad (11)$$

Using the explicit expression (10), we finally obtain,

$$\begin{aligned} P(W, Q) &= \sum_{j,k,l,m} \Delta(W, j, k, l, m, \tau, \gamma) \Delta(Q, j, k, l, m, \tau, \gamma) \\ &\times p_j^0 p_{jk}^{\text{exp}} p_{kl}^{\text{hea}} p_{lm}^{\text{com}}. \end{aligned} \quad (12)$$

For ideal projective measurements, each spectral peak is infinitely sharp ($\gamma = 0$) and the two functions Δ associated with work and heat, $X = (W, Q)$, are simply Dirac peaks, $\Delta(X, j, k, l, m, \tau, 0) = \delta(X - x_{jklm})$, with $w_{jklm} = E_j^0 - E_k^\tau + E_m^\tau - E_l^0$ and $q_{jklm} = E_l^\tau - E_m^\tau$.

In the experiment, each pair of energy measurements is effectively implemented using a Ramsey-like interferometric scheme [27–30]. In this case, spectral peaks have a finite width γ and are well fitted by a Lorentzian distribution, $\Delta(X, j, k, l, m, \tau, \gamma) = 1/\{\pi\gamma[1 + (X - x_{jklm})^2/\gamma^2]\}$ [29, 30]. This is the form we consider in the present experiment.

Joint distribution for work and heat - experiment

We denote the instantaneous energy eigenstates of the two-level system with energy gap $h\nu_i$ ($i = 1, 2$) as $|\Psi_\pm^i\rangle$. The corresponding transition probabilities during expansion and compression strokes are accordingly given by

$$|\langle \Psi_-^1 | U | \Psi_-^2 \rangle|^2 = |\langle \Psi_+^1 | U | \Psi_+^2 \rangle|^2 = 1 - \xi, \quad (13)$$

when there is no transition between states, and by

$$|\langle \Psi_-^1 | U | \Psi_+^2 \rangle|^2 = |\langle \Psi_+^1 | U | \Psi_-^2 \rangle|^2 = \xi. \quad (14)$$

when there is a change of state. The operator U stands for the expansion or compression unitary. Adiabatic driving corresponds to $\xi = 0$.

Table II presents all the sixteen possible combinations for energy transitions of the quantum Otto heat engine during one cycle, together with the respective values of the extracted random values of work and heat.

The reconstructed joint distributions $P(W, Q)$ are displayed in Fig. 6 for the following values of the driving time, $\tau = 200, 260, 320, 260, 420, 500, \text{ and } 700 \mu\text{s}$.

Efficiency distribution

The stochastic efficiency is defined as $\eta = W/Q$. Its distribution may be obtained from the joint distribution $P(W, Q)$, Eq. (12), by integrating over W and Q , as

$$\begin{aligned} P(\eta) &= \int dQ dW \delta\left(\eta - \frac{W}{Q}\right) P(W, Q) \\ &= \sum_{j,k,l,m} p_j^0 p_{jk}^{\text{exp}} p_{kl}^{\text{hea}} p_{lm}^{\text{com}} L(w, q, \gamma, \eta) \end{aligned} \quad (15)$$

with Lorentz-like peaks,

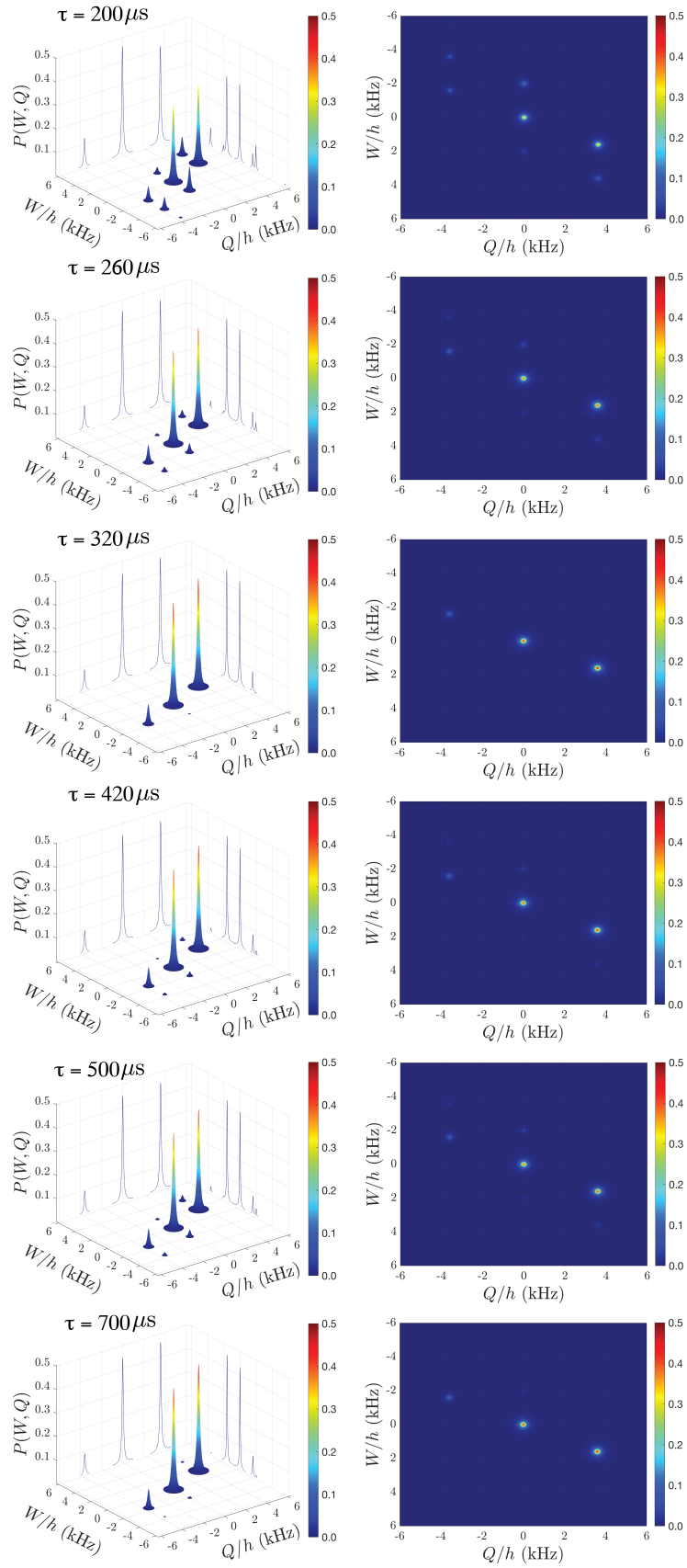


FIG. 6. Reconstructed joint probability distribution for work and heat $P(W, Q)$, Eq. (12), for the following values of the driving times, $\tau = 200, 260, 320, 260, 420, 500, \text{ and } 700 \mu\text{s}$ (left), together with the corresponding density plots (right).

$$\begin{aligned}
L(w, q, \gamma, \eta) = & \frac{\gamma}{\pi^2 (\gamma^2(\eta-1)^2 + \eta^2 q^2 + 2\eta q w + w^2) (\gamma^2(\eta+1)^2 + \eta^2 q^2 + 2\eta q w + w^2)} \\
& \times \left\{ \gamma (-\gamma^2 + \eta^2 (\gamma^2 + q^2) - w^2) (\log(\eta^2) + \log(\gamma^2 + q^2) - \log(\gamma^2 + w^2)) \right. \\
& + 2 \tan^{-1} \left(\frac{q}{\gamma} \right) (\eta^2 q (\gamma^2 + q^2) + 2\eta w (\gamma^2 + q^2) + q (\gamma^2 + w^2)) \\
& \left. + 2 \tan^{-1} \left(\frac{w}{\gamma} \right) (\eta^2 w (\gamma^2 + q^2) + 2\eta q (\gamma^2 + w^2) + w (\gamma^2 + w^2)) \right\} \quad (16)
\end{aligned}$$

where we have dropped the indices of w and q for better readability.

Microscopic versus macroscopic efficiencies

A comparison of the microscopic mean efficiency $\langle \eta \rangle = \langle W/Q \rangle$ and the macroscopic efficiency $\eta_{\text{th}} = \langle W \rangle / \langle Q \rangle$ is displayed in Fig. 7 as a function of the driving time τ . The macroscopic efficiency η_{th} (simulated blue line) increases as the adiabatic regime is approached and irreversible losses induced by quantum friction are reduced. By contrast, the microscopic mean efficiency $\langle \eta \rangle$ (experimental red dots) decreases near the adiabatic regime. It is hence larger for nonadiabatic driving. This counterintuitive behavior is due to the presence of peaks above η_{th} and, thus, to random events that violate the macroscopic second law of thermodynamics.

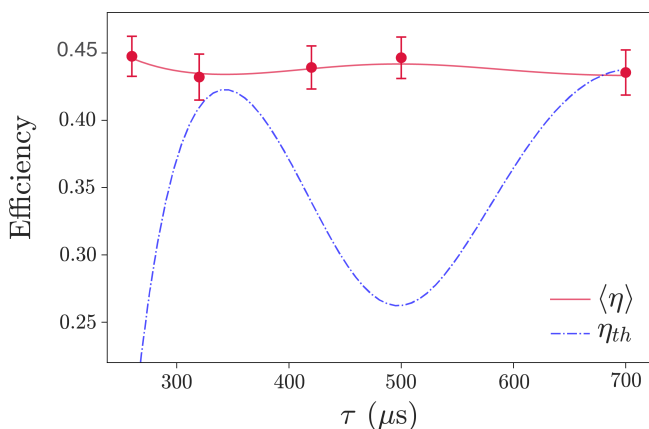


FIG. 7. Comparison of the microscopic mean efficiency $\langle \eta \rangle = \langle W/Q \rangle$ (experimental red dots) and the macroscopic efficiency $\eta_{\text{th}} = \langle W \rangle / \langle Q \rangle$ (simulated blue line) as a function of the driving τ . The macroscopic efficiency increases as the adiabatic regime is approached, while the microscopic average efficiency decreases.

Detailed fluctuation relation

A test of the detailed quantum fluctuation relation,

$$\frac{P(W, Q)}{P(-W, -Q)} = e^{-\Delta\beta Q - \beta_1 W}. \quad (17)$$

was presented in the main text for the driving time $\tau = 200 \mu\text{s}$. Figure 8 exhibits similar tests for $\tau = 200, 260, 260, 320, 420, 500,$ and $700 \mu\text{s}$, showing that the fluctuation theorem for work and heat is obeyed for all the driving times realized in the experiment.

Numerical simulations

The numerical simulation of the experiment was implemented using a python-based code (in-house developed) and QuTiP (the Quantum Toolbox in Python) package [45]. We effectively simulated the finite-time quantum Otto cycle described in the main text with the thermalization strokes being solved using the theoretical thermalization of a qubit with a Markovian thermal reservoir in terms of the Bloch vector components [46]. The time-dependent unitary dynamics of the energy gap expansion and compression strokes were solved numerically. In order to obtain the theoretical transition probability, we ran the simulation from $\tau = 100 \mu\text{s}$ to $\tau = 700 \mu\text{s}$ considering 50 time steps, which was sufficient to generate smooth curves for the theoretical quantities and for the confirmation of the quantum fluctuation relations.

Acknowledgements. We acknowledge financial support from the Federal University of ABC (UFABC), the Brazilian National Council for Scientific and Technological Development (CNPq), the Brazilian Federal Agency for Support and Evaluation of Graduate Education (CAPES), the São Paulo Research Foundation (FAPESP) (Grant number 19/04184-5) and the German Science Foundation (DFG) (Project FOR 2724). This research was performed as part of the Brazilian National Institute of Science and Technology for Quantum Information (INCT-IQ). We also thank the Multiuser Central Facilities of UFABC.

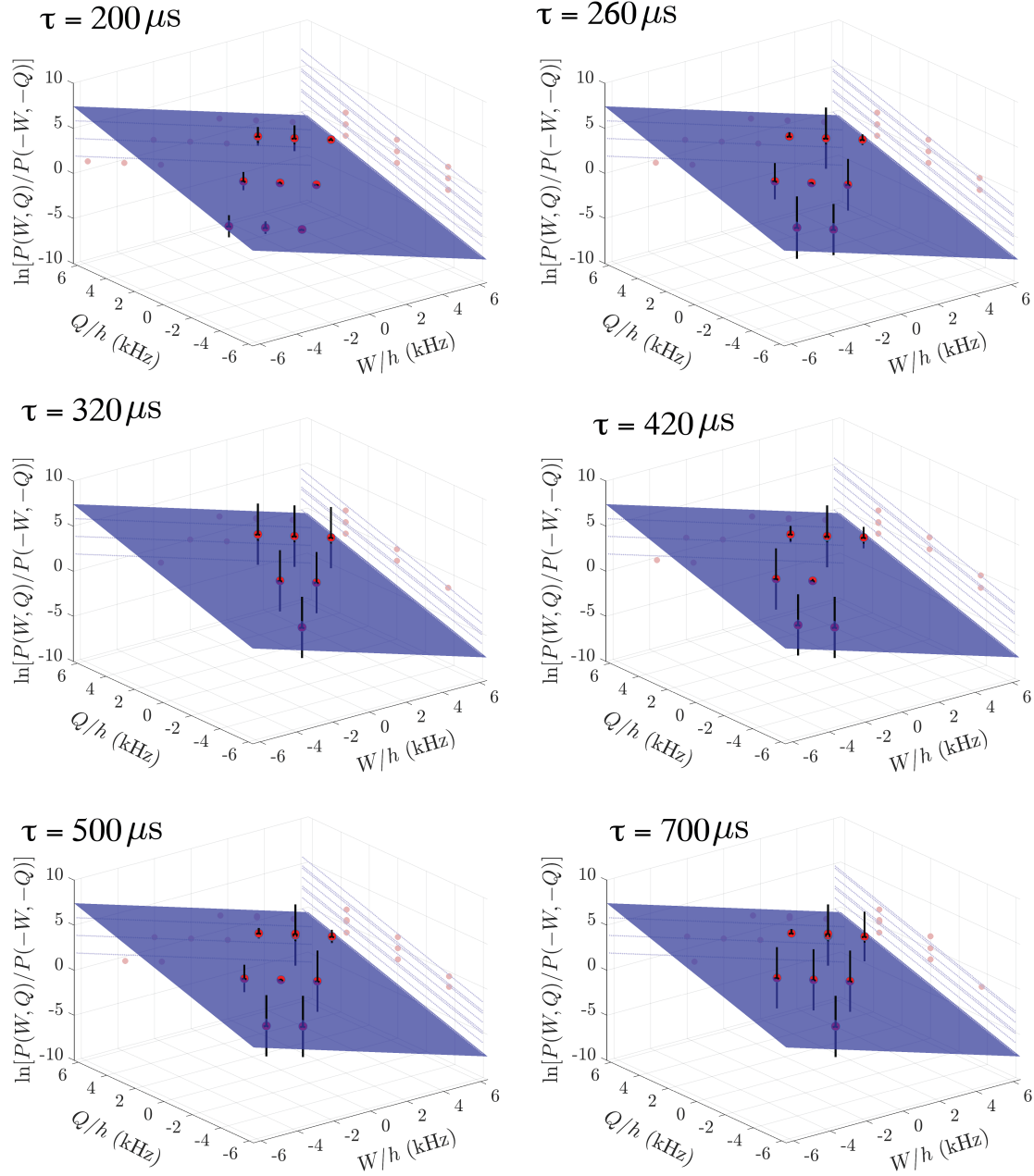


FIG. 8. Experimental verification of the detailed quantum fluctuation relation for work and heat for the following values of the driving time, $\tau = 200, 260, 320, 260, 420, 500,$ and $700 \mu\text{s}$.

-
- [1] Y. A. Cengel and M. A. Boles, *Thermodynamics. An Engineering Approach*, (McGraw-Hill, New York, 2001).
 [2] P. G. Steeneken, K. Le Phan, M. J. Goossens, G. E. J. Koops, G. J. A. M. Brom, C. van der Avoort, and J. T. M. van Beek, Piezoresistive heat engine and refrigerator, *Nature Phys.* **7**, 354 (2011).
 [3] V. Blickle and C. Bechinger, Realization of a micrometre-sized stochastic heat engine, *Nature Phys.* **8**, 143 (2012).
 [4] I. A. Martinez, E. Roldan, L. Dinis, D. Petrov, J. M.

- R. Parrondo and R. A. Rica, Brownian Carnot engine, *Nature Phys.* **12**, 67 (2015).
 [5] K. Proesmans, Y. Dreher, M. Gavrilov, J. Bechhoefer, and C. Van den Broeck, Brownian Duet: A Novel Tale of Thermodynamic Efficiency, *Phys. Rev. X* **6**, 041010 (2016).
 [6] T. Hugel, N. B. Holland, A. Cattani, L. Moroder, M. Seitz, H. E. Gaub, Single-Molecule Optomechanical Cycle, *Science* **296**, 1103 (2002).
 [7] J. Rosnagel, S. T. Dawkins, K. N. Tolazzi, O. Abah, E. Lutz, F. Schmidt-Kaler, and K. Singer, A single-atom heat engine, *Science* **352**, 325 (2016).

- [8] D. von Lindenfels, O. Grab, C. T. Schmiegelow, V. Kaushal, J. Schulz, M. T. Mitchison, J. Goold, F. Schmidt-Kaler and U. G. Poschinger, Spin Heat Engine Coupled to a Harmonic-Oscillator Flywheel, *Phys. Rev. Lett.* **123**, 080602 (2019).
- [9] Y. Zou, Y. Jiang, Y. Mei, X. Guo, and S. Du, Quantum Heat Engine Using Electromagnetically Induced Transparency, *Phys. Rev. Lett.* **119**, 050602 (2017).
- [10] J. Klatzow, J. Becker, P. Ledingham, C. Weinzetl, K. Kaczmarek, D. Saunders, J. Nunn, I. Walmsley, R. Uzdin, E. Poem, Experimental Demonstration of Quantum Effects in the Operation of Microscopic Heat Engines, *Phys. Rev. Lett.* **122**, 110601 (2019).
- [11] R. J. de Assis, T. M. de Mendonca, C. J. Villas-Boas, A. M. de Souza, R. S. Sarthour, I. S. Oliveira and N. G. de Almeida, Efficiency of a Quantum Otto Heat Engine Operating Under a Reservoir at Effective Negative Temperatures, *Phys. Rev. Lett.* **122**, 240602 (2019).
- [12] J. P. S. Peterson, T. B. Batalhão, M. Herrera, A. M. Souza, R. S. Sarthour, I. S. Oliveira and R. M. Serra, Experimental Characterization of a Spin Quantum Heat Engine, *Phys. Rev. Lett.* **123**, 240601 (2019).
- [13] N. Van Horne, D. Yum, T. Dutta, P. Hänggi, J. Gong, D. Poletti and M. Mukherjee, Single-atom energy-conversion device with a quantum load, *npj Quantum Information* **6**, 37 (2020).
- [14] Q. Bouton, J. Nettersheim, S. Burgardt, D. Adam, E. Lutz, and A. Widera, A quantum heat engine driven by atomic collisions, *Nature Comm.* **12**, 2063 (2021).
- [15] U. Seifert, Stochastic thermodynamics, fluctuation theorems and molecular machines, *Rep. Prog. Phys.* **75**, 126001 (2012).
- [16] M. Esposito, U. Harbola and S. Mukamel, Nonequilibrium fluctuations, fluctuation theorems, and counting statistics in quantum systems, *Rev. Mod. Phys.* **81**, 1665 (2009).
- [17] M. Campisi, P. Hänggi, and P. Talkner, Quantum Fluctuation Relations: Foundations and Applications, *Rev. Mod. Phys.*, **83** 771 (2011).
- [18] G. Verley, M. Esposito, T. Willaert, and C. Van den Broeck, The unlikely Carnot efficiency, *Nature Commun.* **5**, 4721 (2014).
- [19] M. Poletti, G. Verley, and M. Esposito, Efficiency Statistics at All Times: Carnot Limit at Finite Power, *Phys. Rev. Lett.* **114**, 050601 (2015).
- [20] J. Jiang, B. K. Agarwalla and D. Segal, Efficiency Statistics and Bounds for Systems with Broken Time-Reversal Symmetry, *Phys. Rev. Lett.* **115**, 040601 (2015).
- [21] S. K. Manikandan, L. Dabelow, R. Eichhorn and S. Krishnamurthy, Efficiency Fluctuations in Microscopic Machines, *Phys. Rev. Lett.* **122**, 140601 (2019).
- [22] N. A. Sinitsyn, Fluctuation relation for heat engines, *J. Phys. A: Math. Theor.* **44**, 405001 (2011).
- [23] S. Lahiri, S. Rana, A. M. Jayannavar, Fluctuation relations for heat engines in time-periodic steady states, *J. Phys. A* **45**, 465001 (2012).
- [24] M. Campisi, Fluctuation relation for quantum heat engines and refrigerators, *J. Phys. A* **47**, 245001 (2014).
- [25] R. Kosloff and Y. Rezek, The Quantum Harmonic Otto Cycle, *Entropy* **19**, 136 (2017).
- [26] I. S. Oliveira, T. J. Bonagamba, R. S. Sarthour, J. C. C. Freitas, and E. R. deAzevedo, *NMR Quantum Information Processing*, (Elsevier, Amsterdam, 2007).
- [27] R. Dorner, S. R. Clark, L. Heaney, R. Fazio, J. Goold, and V. Vedral, Extracting Quantum Work Statistics and Fluctuation Theorems by Single-Qubit Interferometry, *Phys. Rev. Lett.* **110**, 230601 (2013).
- [28] L. Mazzola, G. De Chiara, and M. Paternostro, Measuring the Characteristic Function of the Work Distribution, *Phys. Rev. Lett.* **110**, 230602 (2013).
- [29] T. B. Batalhão, A. M. Souza, L. Mazzola, R. Auccaise, R. S. Sarthour, I.S. Oliveira, J. Goold, G. De Chiara, M. Paternostro, and R. M. Serra, Experimental Reconstruction of Work Distribution and Study of Fluctuation Relations in a Closed Quantum System, *Phys. Rev. Lett.* **113**, 140601 (2014).
- [30] T. B. Batalhão, A. M. Souza, R. S. Sarthour, I. S. Oliveira, M. Paternostro, E. Lutz, R. M. Serra, Irreversibility and the Arrow of Time in a Quenched Quantum System. *Phys. Rev. Lett.* **115**, 190601 (2015).
- [31] C. Van den Broeck, Thermodynamic Efficiency at Maximum Power, *Phys. Rev. Lett.* **95**, 190602 (2005).
- [32] M. Esposito, K. Lindenberg, and C. Van den Broeck, Universality of Efficiency at Maximum Power, *Phys. Rev. Lett.* **102**, 130602 (2009).
- [33] B. Cleuren, B. Rutten, and C. Van den Broeck, Universality of efficiency at maximum power, *Eur. Phys. J. Special Topics* **224**, 879 (2015).
- [34] M. Sune and A. Imparato, Efficiency fluctuations in steady-state machines, *J. Phys. A* **52**, 045003 (2019).
- [35] R. Kosloff and T. Feldmann, Discrete four-stroke quantum heat engine exploring the origin of friction, *Phys. Rev. E* **65**, 055102(R) (2002).
- [36] T. Feldmann and R. Kosloff, Quantum four-stroke heat engine: Thermodynamic observables in a model with intrinsic friction, *Phys. Rev. E* **68**, 016101 (2003).
- [37] F. Plastina, A. Alecce, T. J. G. Apollaro, G. Falcone, G. Francica, F. Galve, N. Lo Gullo, and R. Zambrini, Irreversible Work and Inner Friction in Quantum Thermodynamic Processes, *Phys. Rev. Lett.* **113**, 260601 (2014).
- [38] K. Micadei, J. Peterson, A. Souza, R. Sarthour, I. Oliveira, G. Landi, T. Batalhão, R. Serra, and E. Lutz, Reversing the direction of heat flow using quantum correlations, *Nature Comm.* **10**, 2456 (2019).
- [39] C. Jarzynski, H. T. Quan, and S. Rahav, Quantum-Classical Correspondence Principle for Work Distributions *Phys. Rev. X* **5**, 031038 (2015).
- [40] P. Talkner, E. Lutz, and P. Hänggi, Fluctuation theorems: Work is not an observable, *Phys. Rev. E* **75**, 050102(R) (2007).
- [41] R. J. Barlow, *Statistics*, (Wiley, New York, 1989).
- [42] T. Denzler and E. Lutz, Efficiency statistics of a quantum heat engine, *Phys. Rev. Research* **2**, 032062(R) (2020).
- [43] C. Jarzynski and D. K. Wójcik, Classical and Quantum Fluctuation Theorems for Heat Exchange, *Phys. Rev. Lett.* **92**, 230602 (2004).
- [44] A. Papoulis, *Probability, Random Variables and Stochastic Processes*, (McGraw-Hill, New York, 1991).
- [45] QuTiP: Quantum Toolbox in Python (4.1), <http://qutip.org/>.
- [46] S. Chakraborty, P. Cherian J, and S. Ghosh, On thermalization of two-level quantum systems, *EPL* **126**, 40003 (2019).